Chinese Chemical Letters 35 (2024) 109441

Contents lists available at ScienceDirect

Chinese Chemical Letters

journal homepage: www.elsevier.com/locate/cclet

Two birds with one stone: Functionalized wood composites for efficient photocatalytic hydrogen production and solar water evaporation

Deqi Fan[a,1], Yicheng Tang[b,1], Yemei Liao[b], Yan Mi[c], Yi Lu[b,*], Xiaofei Yang[a,b,c,*]

[a] College of Chemical Engineering, Nanjing Forestry University, Nanjing 210037, China
[b] Jiangsu Co-Innovation Center of Efficient Processing and Utilization of Forest Resources, International Innovation Center for Forest Chemicals and Materials, College of Science, Nanjing Forestry University, Nanjing 210037, China
[c] Key Laboratory of Chemistry and Engineering of Forest Products, State Ethnic Affairs Commission, Guangxi Key Laboratory of Chemistry and Engineering of Forest Products, Guangxi Minzu University, Nanning 530006, China

ARTICLE INFO

Article history:
Received 25 June 2023
Revised 8 December 2023
Accepted 20 December 2023
Available online 23 December 2023

Keywords:
Photocatalysis
Photothermal
Nb_2C MXene
g-C_3N_4
Wood

ABSTRACT

Maximizing solar energy utilization is a persistent challenge in photo catalysis, which determines sustainable solar-driven photocatalytic process. Photo thermal-coupled photo catalysis is considered as a promising solution to tackle the issues of sustainable energy scarcity and environmental pollution by harvesting the full-spectrum solar energy. Herein, a highly efficient photo thermal-accelerated photo catalysis system is elaborately established, in which the assembled carbonized stick/Nb_2C MXene evaporator can heat water into vapor and the integrated g-C_3N_4 photocatalyst further enables high-efficiency photocatalytic hydrogen production. The designed hyperboloid wood-based architecture possesses a multiphase interface of water steam/catalyst/hydrogen to reduce the transport resistance of hydrogen gas in liquid and ultimately maximize the output of hydrogen energy. Consequently, this coupled photothermal-photocatalytic system achieves a stable solar evaporation rate of 2.16 kg m^{-1} h^{-1} under one sun irradiation and highly efficient hydrogen-evolving rate of 3096 μmol g^{-1} h^{-1}. This work paves a way to explore the improvement of photocatalytic hydrogen production by synergic photothermal effect for potential applications in renewable solar energy utilization and hydrogen production.

Solar energy is considered as an inexhaustible source for energy conversion development due to its abundant reserves and renewable capacity. The efficient utilization of sustainable solar technology is of great significance in mitigating freshwater scarcity and the energy crisis [1,2]. Photothermal and photocatalytic hydrogen production are two ubiquitous schemes for solar energy utilization. Photothermal conversion technology is a direct approach to capture and utilize solar energy for achieving available thermal energy [3,4]. Photocatalytic conversion normally involves capturing solar energy to evolve hydrogen energy with high combustion calorific value [5]. Nevertheless, the non-directional conversion between solar and thermal energy inevitably weakened its capture of high-frequency ultraviolet spectra [6,7]. Coincidentally, due to the limitation of the energy band structure of the semiconductor photocatalysts, traditional photocatalytic hydrogen production can only utilize limited high-frequency solar spectrum (generally < 600 nm) [8]. Consequently, to maximize the overall solar energy utilization, the rational and efficient design of photothermal-photocatalytic synergistic system that can targetedly absorb different frequencies of solar photons, is extremely critical.

The natural-derived porous wood has become an ideal substrate material on account of the exclusive microchannels for water transmission, low thermal conductivity, and easy processing characteristics [9–11]. Wood-based solar system can be endowed with multifunctional characteristics *via* surface carbonization or coating solar absorption materials such as carbon-based materials, metal plasma nanomaterials, and semiconductors [12–14]. Graphitic carbon nitride (g-C_3N_4), as a typical two-dimensional semiconductor material, has triggered extensive concerns in photocatalytic water splitting owing to its moderate bandgap, non-toxicity, excellent stability, and low cost [15]. However, the rapid recombination of photogenerated carriers on single-component g-C_3N_4 and easy agglomeration of g-C_3N_4 greatly impede the process of photocatalysis hydrogen production [16]. Typically, integrating appro-

* Corresponding authors.
E-mail addresses: yilu@njfu.edu.cn (Y. Lu), xiaofei.yang@njfu.edu.cn (X. Yang).
[1] These authors contributed equally to this work.

https://doi.org/10.1016/j.cclet.2023.109441
1001-8417/

priate co-catalysts with g-C_3N_4 has been demonstrated as a reasonable and efficient strategy to improve the photocatalytic activity of g-C_3N_4 [17,18]. Nb_2C MXene, as an effective co-catalyst, has aroused remarkable attention owing to excellent conductivity, hydrophilicity, and low Fermi level [19,20]. Through hydrophilic functional groups on the layered surface, Nb_2C can readily form close connections with various semiconductors. The Schottky barrier at the coupling interface between Nb_2C and semiconductor can be used as an electron reservoir to promote the separation of photoinduced electrons and holes [21,22]. Moreover, remarkable metal conductivity of Nb_2C enables the rapid separation of photogenerated carriersm, and the two-dimensional layered structure of Nb_2C can provide abundant active catalytic sites and further improve the photocatalytic performance of g-C_3N_4. Accordingly, to promote and optimize the utilization of the solar full spectrum, the reasonably assembled of photocatalysis system (g-C_3N_4 catalyst and MXene co-catalyst) and photothermal system (wood substrate) is highly desirable for capturing solar photons of different wavelengths.

Herein, inspired by the synergy of solar-driven photo catalysis and photo thermal effect, a novel assembled hyperboloid wood-based system is elaborately designed, which effectively integrates hydrogen-evolving photo catalyst g-C_3N_4 with nanostructured Nb_2C that acts as co-catalyst and also possesses photo thermal effect to simultaneously drive the removal of hydrogen production and solar steam generation with high efficiency. Nb_2C-g-C_3N_4 is a MXene-derived heterojunction, in which Nb_2C is *in-situ* anchored on porous g-C_3N_4 *via* the NHx-Nb bond, has been adhered tightly on the wood superficies by chemical cross-linking. The specialized designs of catalyst loading in wood surface ingeniously confine the Nb_2C-g-C_3N_4 at the water/air interface to implement thermal localization, which enormously reduce the heat loss of bulk water. The annular tilt structure on the surface of the hyperbolic evaporator can enable the evaporator to effectively capture multi-angle solar photons. Moreover, the temperature difference between the upper and bottom Hyperboloid regions forms air convection, accelerating the generation of steam. The regional high concentration steam flow can be splitted into hydrogen by the catalyst loaded on the surface of the stick, forming a mixed multiphase interface of steam/catalyst/hydrogen and water/catalyst/hydrogen. This multiphase photocatalytic-photo thermal system reduces the transmission resistance of hydrogen and the barrier of solid-liquid interface, thus improving the photocatalytic hydrogen production rate.

Benefiting from the materials selection and structure-guided rational design, the resulting hyperboloid-shaped wood-based multifunctional system (S-NC-CW) achieves a high solar evaporation rate of 2.16 kg m^{-1} h^{-1}, and acquires an efficient hydrogen-evolving rate of 3096 μmol g^{-1} h^{-1}. Such an integrated system of solar evaporation and photocatalytic hydrogen evolution highlighted the seamless integration of water, solar energy, and fuel, opening a window for comprehensive application of solar energy technology.

The design procedure of a wood-based system for solar-driven water-heat-hydrogen production is graphically portrayed in Fig. 1. Namely, NC-CW system is conceptually assembled with photothermal and catalytic Nb_2C-g-C_3N_4 nanoparticles and natural water-receptive wood stick substrates. The Nb_2C-g-C_3N_4 nanoparticles efficient solar-hydrogen conversion with laminar g-C_3N_4 as photo-redox main catalyst and Nb_2C nanosheets as auxiliary catalyst for enhancing photogenerated electron-hole pair separation. Nb_2C nanosheets are synthesized by etching and exfoliation of bulk Nb_2AlC (MAX) (Fig. S1a in Supporting information). As shown in Fig. 2a, Figs. S1b and c (Supporting information), the Al atomic layer inside the precursor MAX was selectively etched and separated to form multilayer accordion-like MXene *via* the simultaneous action of NH_4F and HCl. Afterwards, the interlayer spacing of MXene was enlarged by the intercalation of tetrapropylammonium hydroxide (TPAOH) and ultrasonication sonication under N_2 atmosphere, then the thin layers or single layer of Nb_2C was obtained and served as a platform for the growth of g-C_3N_4. Eventually, the flake-like g-C_3N_4 (Fig. 2b) was successfully *in-situ* grown on Nb_2C nanosheets by electrostatic self-assembly of precursors and high-temperature calcination. The composite microstructure morphology and phase composition of Nb_2C-g-C_3N_4 was observed by SEM and TEM. As demonstrated in Figs. 2c and d, two different species of thin nanosheets stacked with each other. Moreover, the locally amplified transmission image (yellow box) further demonstrated the obvious interface connection between Nb_2C and g-C_3N_4 nanosheets (Figs. 2e and f). The obvious lattice spacing of 0.27 nm was assigned to the (042) plane of Nb_2C, while the amorphous region was pertained to g-C_3N_4 [23]. Moreover, the energy-dispersive X-ray spectroscopy (EDX) mapping images in Fig. 2g revealed the uniform distribution of C, N and Nb elements in the nanosheets, which further manifested the *in-situ* growth of g-C_3N_4 on Nb_2C sheet. In addition, the surface morphology and element distribution of NC-2 coated carbonized stick (NC-CW) are shown in Fig. 2h,

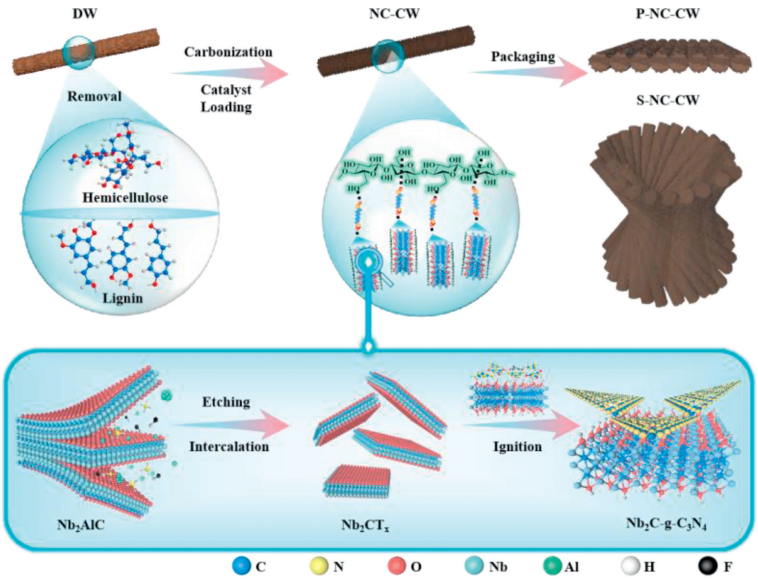

Fig. 1. Synthesis process of assembled hyperboloid wood-based bifunctional system.

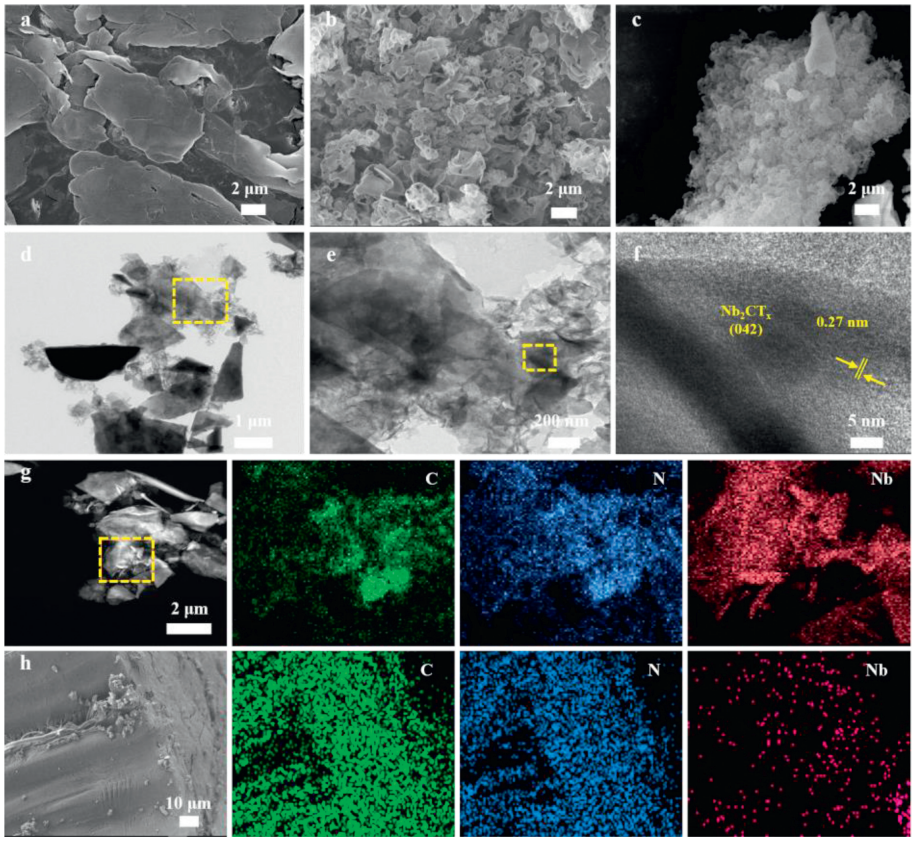

Fig. 2. (a) The magnification SEM of the Nb_2C. (b) The magnification SEM of the g-C_3N_4. (c) The magnification SEM of the NC-2. (d-f) TEM images of NC-2. (g) The corresponding energy dispersive spectrometer (EDS) elemental maps of C, N, and Nb in NC-2. (h) The magnification SEM of the NC-CW and the corresponding energy dispersive spectrometer (EDS) elemental maps of C, N and Nb.

which revealed the close adhesion of Nb_2C-g-C_3N_4 nanoparticles on the stick surface. Furthermore, the dual phase characterization of XRD and XPS further validated the successful *in-situ* recombination of Nb_2C-g-C_3N_4. For Nb_2C MXene, the strongest diffraction peak (103) located at 38.8° completely disappeared after etching, confirming the removal of Al layer [24,25]. Meanwhile, the (002) peak corresponding to the main crystal plane shifted from 12.76° to 7.56°, which indicated the increase of interlayer distance and the successful exfoliation of thin Nb_2C nanosheets [26]. Besides, the synthesized Nb_2C-g-C_3N_4 demonstrated the diffraction peaks of Nb_2C and g-C_3N_4, indicating the efficacious structural coupling of the two components (Fig. 3a), which was consistent with full-scale XPS survey spectrum in Fig. 3b. The XPS spectra of different catalysts in the C 1s, O 1s, and Nb 3d regions were deconvoluted and were demonstrated in Fig. 3c. For C 1s spectrum, the peaks in g-C_3N_4 located at 284.3 eV, 285.8 eV, and 287.6 eV correspond to C–C, C–NHx, and N-C=N, respectively [27,28]. After compounded with Nb_2C, the peaks ascribed to C–C, C–NHx, and N-C=N shifts to the lower energies, which manifested the formation of composite interface between the two components. Meanwhile, the N 1s high-resolution spectra of Nb_2C-g-C_3N_4 also showed a negative shift for the C-N=C in the triazine ring, N-$(C)_3$, C-NH_3, and π-excitation relative peaks to bare g-C_3N_4, which further affirmed the carrier migration and interface interaction from Nb_2C and g-C_3N_4. Besides, the Nb 3d spectra of NC-2 can be deconvoluted into four main peaks at 203.3, 204.7, and 209.4 eV which correspond to the $Nb3d_{5/2}$, $Nb3d_{5/2}$, and Nb-C, respectively [29,30]. In comparison with pure Nb_2C, all the Nb-related peaks in the NC-2 exhibit an obvious shift to higher energies, which could be attributed to the electronic migration by Schottky interfaces between the Nb_2C and g-C_3N_4 atoms and resulted in the generation of the heterojunction. Subsequently, the isocyanate coated on the surface of the stick was condensed under ultraviolet light, and then heterojunction photocatalyst was successfully attached to the stick surface through the polyurethane bond, as shown in the infrared absorption bands at 827 cm^{-1} and 1234 cm^{-1} (Fig. S1d in Supporting information) [31].

Apart from the phase validation of the catalyst heterojunction, the hydrophilicity and optical characteristic of the wood-based system were further investigated to expound its feasibility for solar multifunctional applications. As shown in Fig. S2a (Supporting information), the NC-CW after carbonization and catalyst loading still inherited excellent wettability of wood, which guaranteed the rapid transmission of water from the bottom to the solar evaporation interface. Besides, solar absorbance of different systems was determined based on the integral fitting of the UV–vis-NIR diffusive spectra within the wavelength range of 400–2500 nm (Fig. S2b in Supporting information). The average solar absorption of DW, CW, NC-DW, and NC-CW was 85.9%, 91.1%, 85.5%, and 90.5%, respectively. Owing to the high solar absorptivity, the average optical-contact surface temperature of the dried NC-DW was markedly increased up to 55.2 °C within 10 min under one sun illumination and finally reached a steady state temperature of about 58.4 °C after 60 min (Figs. S2c and d in Supporting information). Subsequently, the wooden sticks were woven into raft and hyperboloid shapes through different copper wire weaving processes (Fig. S3a in Supporting information). The catalyst particles on the surface of the self-assembled wood stick vertical evaporator did not occur obvious shedding phenomenon during the long-term water immersion process, which further verified the stability of the catalytic adhesion layer (Fig. S3b in Supporting information). Noticeably, the bottom water could be continuously transported to the top of the S-NC-CW *via* the natural transmission channel,

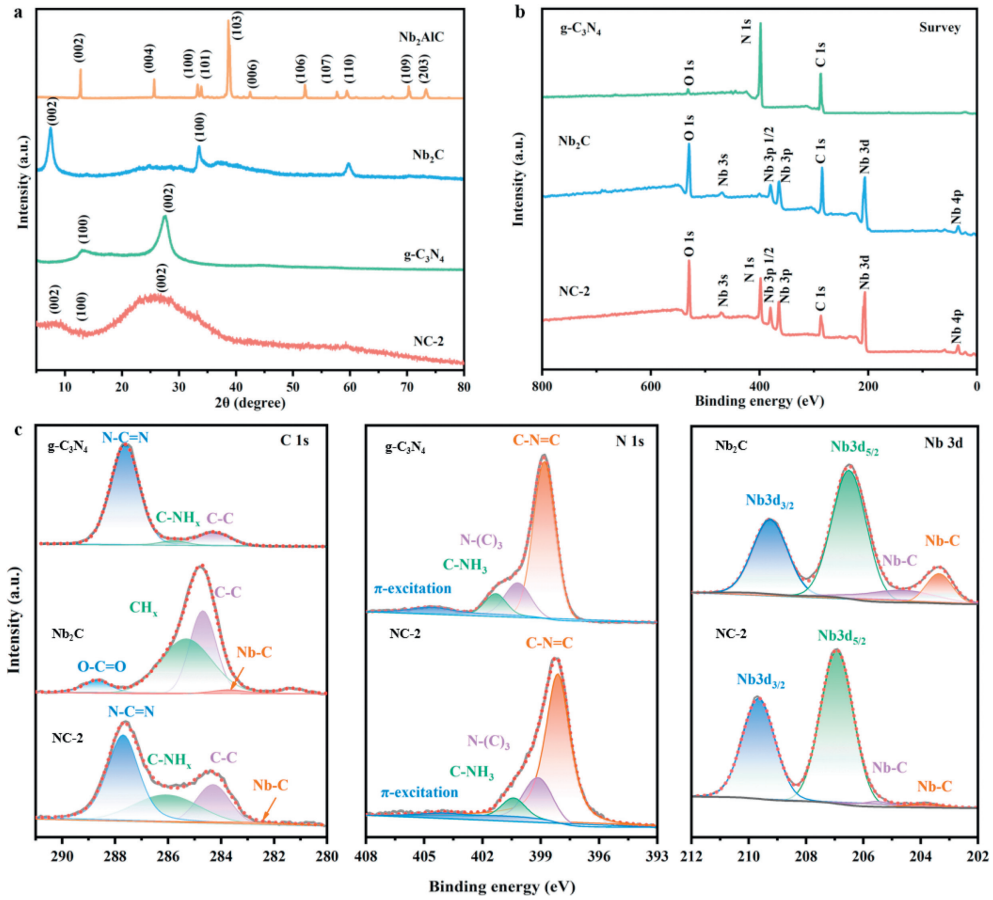

Fig. 3. (a) XRD spectra of Nb_2AlC, Nb_2C, g-C_3N_4, and NC-2. (b) Survey spectrum of g-C_3N_4, Nb_2C, and NC-2 and high-resolution spectra of (c) C 1s, N 1s, and Nb 3d.

which could be testified by the side views of infrared thermal images within one hour (Fig. S3c in Supporting information). The superior solar absorption characteristics along with the excellent photothermal conversion made the assembled stick system an ideal candidate for solar multi-functional applications.

The solar evaporation performance of the assembled stick system could be evaluated by recording the weight loss of water with constant time interval under simulated solar sources. The specific experimental device was schematically shown in Fig. 4a. The water evaporation rates of the P-NC-DW, P-NC-CW, S-NC-DW, and S-NC-CW under one sun irradiation were determined to be 1.70, 2.06, 1.86, and 2.16 kg m^{-2} h^{-1} after 10 min evaporation stabilization (Fig. 4b). Ultrafast water evaporation was attributed to the reduction of evaporation enthalpy in delignified wood, as confirmed by the dark field experiment [28]. The measured equivalent water vaporization enthalpy for DW, CW, NC-DW, and NC-CW were 1590, 1610, 1480, and 1502 J^{-1} g^{-1}, respectively (Fig. S4a in Supporting information). Furthermore, the energy conversion efficiency (η) of the evaporators could be further calculated by the measured evaporation rate and evaporation enthalpy [32]. The calculated energy conversion efficiencies of P-NC-DW, P-NC-CW, S-NC-DW, and S-NC-CW were 75.05%, 92.35%, 82.35%, and 95.56%, respectively (Fig. S4b in Supporting information), and the solar water evaporation performance of the S-NC-CW was superior to the reported wood-based evaporation systems [33–41] (Table S1 and Fig. S4c in Supporting information). Meanwhile, the evaporation rate of S-NC-CW remained almost unchanged in 10 evaporation cycles, showing stable and efficient solar evaporation performance (Fig. S4d in Supporting information). Furthermore, we have conducted the outdoor test under natural sunlight for investigating the practical solar evaporation performance of the S-NC-CW solar absorber. As shown in Fig. S5 (Supporting information), the outdoor evaporation experiment was carried out in a typical sunny environment in Nanjing, China. The environmental temperature, humidity, solar intensity, atmosphere pressure, and wind velocity were recorded in real time every half hour. The average solar flux during the outdoor test was 0.52 kW^{-1} m^{-1}, and the average evaporation rate of the device was 1.1 kg m^{-1} h^{-1} over the outdoor practical test. Therefore, S-NC-CW was selected as the optimum material for further research in solar multifunctional system.

Based on the above efficient solar photothermal performance of evaporators, integrating photocatalytic hydrogen production with photothermal effect would enormously expand the multifunctional utilization of wood-based system. The hydrogen evolution performance of Nb_2C-g-C_3N_4 photocatalysts and assembled stick evaporators under simulated solar irradiation was examined to validate the possibility of cooperative photothermal-photocatalytic application. As demonstrated in Figs. S6a and b (Supporting information), the pristine g-C_3N_4 revealed limited photocatalytic hydrogen evolution performance (605 μmol g^{-1} h^{-1}), attributing to its poor charge separation rate. As expected, the admission of Nb_2C significantly improved the photocatalytic activity of the catalyst, with the highest photocatalytic hydrogen production rate (3617 μmol g^{-1} h^{-1}) when the molar ratio of g-C_3N_4 to Nb_2C was 100, 6 times higher than pure g-C_3N_4 (NC-0). Highly conductive Nb_2C accepted and transmitted the electrons to suppress electron diffusion and accelerate the separation of photogenerated carriers. Furthermore, excessive Nb_2C content in NC-3 was prone to stack agglomeration, which reduced the contact area with g-C_3N_4, and ultimately weakened the ability of charge transfer and the

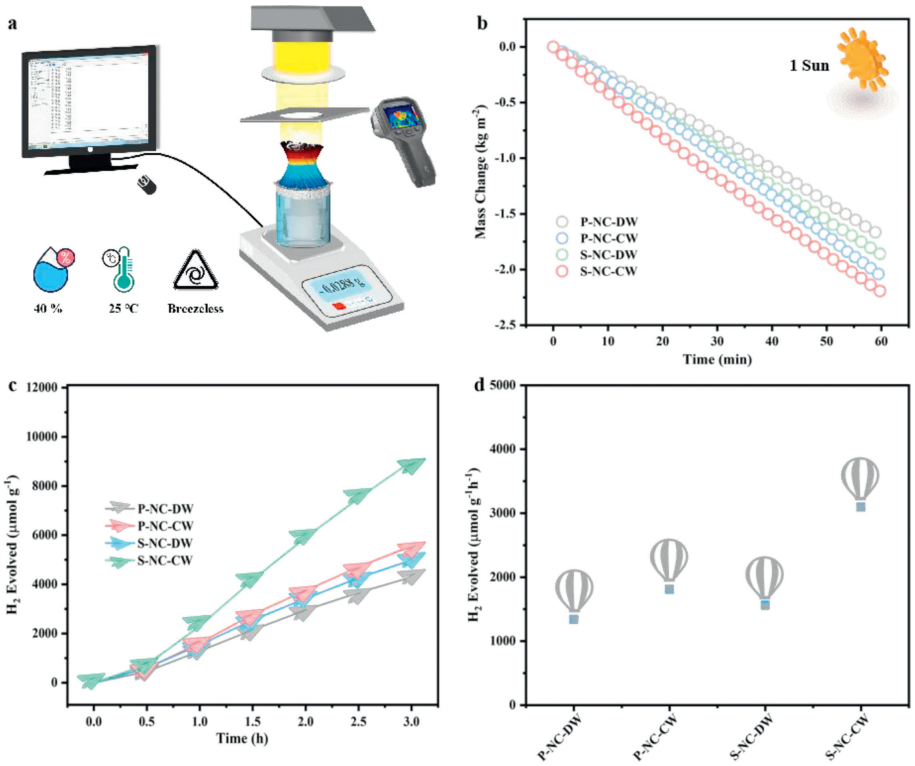

Fig. 4. (a) Schematic illustration of the equipment of solar evaporation. (b) The mass loss of water over time. (c) Time-course hydrogen evolution performance and (d) corresponding hydrogen evolution rates of P-NC-DW, P-NC-CW, S-NC-DW, and S-NC-CW.

photocatalytic performance of heterojunction. Therefore, NC-2 heterojunction catalyst was eventually selected to coat on the stick surface for endowing additional photocatalytic performance. On the one hand, the synergistic effect of photo thermal effect on photo catalysis could be clearly examined by coating NC-2 catalyst on the wood substrate with different carbonization states (Figs. 4c and d, Fig. S6c in Supporting information). On the other hand, by comparing the hydrogen production effect on the self-assembled evaporators with the plane and vertical structure, the localized high-concentration steam generated by the multiphase system in the vertical hyperboloid structure could significantly accelerate photocatalytic hydrogen production. Ultimately, the hydrogen evolution of the S-NC-CW could be significantly further improved to 3096 μmol g^{-1} h^{-1}. In addition, the cycle durability of the S-NC-CW under continuous sunlight irradiation further verified its stable photocatalytic hydrogen production performance (Fig. S7a in Supporting information). Moreover, we have detected the phase of the catalyst after long-term photocatalytic reaction by SEM and XRD. As shown in Fig. S7b (Supporting information), characteristic peaks of Nb_2C and C_3N_4 were still existed in the NC-2 catalyst after long-term photo thermal and photocatalytic reaction. Meanwhile, the morphology of NC-2 has no significant change by scanning electron microscopy after long-term photo thermal and photocatalytic reaction, which further verified the stability of the Nb_2C-C_3N_4 catalyst (Fig. S7c in Supporting information).

To better clarify the superiority of NC-2 photocatalytic activity, the catalytic properties of g-C_3N_4 and NC-2 were compared and analyzed by the electrochemical impedance spectra and transient photocurrent response under visible light illumination. As shown in Fig. S8a (Supporting information), the curvature diameter of semicircle was proportional to charge transfer resistance of photo catalyst [42]. The smaller circular segment span of NC-2 heterojunction demonstrated the smaller charge-transfer resistance compared with pure g-C_3N_4. Similarly, NC-2 illustrated the higher intensity of photocurrent cyclic signal in Fig. S8b (Supporting information), corresponding to the optimized separation efficiency of photo excited electron-hole pairs [43,44]. The optimization of the heterojunction performance was attributed to the strong interaction between Nb_2C and g-C_3N_4 interfaces, which accelerated the charge separation and transfer during the formation of Schottky junction. Additionally, the actual band structure of Nb_2C-g-C_3N_4photo catalyst could be calculated by UV–vis diffuse reflectance spectroscopy and Mott–Schottky curve [45,46]. The Tafel curves converted by the diffuse reflection spectrum conversion revealed that the band gaps of g-C_3N_4 were 2.69 eV (Fig. S8c in Supporting information). The amalgamation of Nb_2C into g-C_3N_4 significantly reduced the band gap (E_g), attributing to the intensified visible light absorption capacity of the composite materials relative to the individual g-C_3N_4 (Fig. S8d in Supporting information). Moreover, the flat-band potential (E_{fb}) of g-C_3N_4 in the Mott–Schottky plot was −1.12 V *versus* Ag/AgCl, corresponding to −0.51 V *versus* normal hydrogen electrode (*vs.* NHE) [47] (Fig. S8e). Typically, the conduction band potential (CB) was higher than E_{fb} (NHE) of n-type semiconductor for 0.3 eV [48]. Thus, the CB of g-C_3N_4 was −0.81 V (*vs.* NHE), and the valence band potential (VB) was 1.90 V (*vs.* NHE) calculating by band gap (2.74 eV) of g-C_3N_4 (Fig. S8f).

In summary, the hyperboloid-shaped wood-based multifunctional system (S-NC-CW) was successfully assembled by surface carbonization and catalyst loading. The S-NC-CW system was customized with broadband solar absorption, excellent inbuilt water transmission structure, and efficient photocatalytic activity which would be desirable for high solar-to-thermal conversion and excellent catalytic hydrogen generation. The water evaporation rates of the S-NC-CW could reach up to 2.16 kg m^{-1} h^{-1} under one sun irradiation, corresponding to the efficient energy conversion efficiency of 95.56%. Moreover, the gaseous water molecules generated by evaporation were decomposed into hydrogen through the Nb_2C-

g-C_3N_4 catalyst attached to the stick surface, and the hydrogen evolution could be significantly further optimized to 3096 μmol g^{-1} h^{-1} by synergistic promotion of photothermal effect. This solar-to-energy multifunctional conversion system provides an advisable approach for addressing the issues of worldwide renewable energy and freshwater scarcity.

Declaration of competing interest

The authors declare that they have no known competing financial interests or personal relationships that could have appeared to influence the work reported in this paper.

Acknowledgments

This work was financially supported by the National Natural Science Foundation of China (No. 51902164), Key Laboratory of Chemistry and Engineering of Forest Products, State Ethnic Affairs Commission, Guangxi Key Laboratory of Chemistry and Engineering of Forest Products (No. GXFK2207), Guangxi Minzu University, and Science Fund for Distinguished Young Scholars (No. JC2019002), Nanjing Forestry University. This work was also funded by the Priority Academic Program Development of Jiangsu Higher Education Institutions (PAPD) and Postgraduate Research &Practice Innovation Program of Jiangsu Province (No. KYCX22_1089).

Supplementary materials

Supplementary material associated with this article can be found, in the online version, at doi:10.1016/j.cclet.2023.109441.

References

[1] T. Ding, G.W. Ho, Joule 5 (2021) 1639–1641.
[2] Y. Wang, W. Zhao, M. Han, J. Xu, K.C. Tam, Nature Water 1 (2023) 587–601.
[3] X. Wu, Z. Wu, Y. Wang, et al., Adv. Sci. 8 (2021) 2002501.
[4] X. Min, B. Zhu, B. Li, J. Li, J. Zhu, Acc. Mater. Res. 2 (2021) 198–209.
[5] C. Zhao, C. Han, X. Yang, J. Xu, Green Chem. 24 (2022) 4728–4741.
[6] D. Fan, Y. Lu, H. Zhang, et al., Appl. Catal. B: Environ. 295 (2021) 120285.
[7] Y. Lu, H. Zhang, D. Fan, Z. Chen, X. Yang, J. Hazard. Mater. 423 (2022) 127128.
[8] S.W.L. Ng, M. Gao, W. Lu, M. Hong, G.W. Ho, Adv. Funct. Mater. 31 (2021) 2104750.
[9] G. Chen, T. Li, C. Chen, et al., ACS Nano 15 (2021) 11244–11252.
[10] Y. Chen, J. Yang, L. Zhu, et al., J. Mater. Chem. A 9 (2021) 15482–15492.
[11] S. Xiao, C. Chen, Q. Xia, et al., Science 374 (2021) 465–471.
[12] Y. Lu, D. Fan, Z. Shen, et al., Nano Energy 95 (2022) 107016.
[13] Q. Xia, C. Chen, T. Li, et al., Sci. Adv. 7 (2021) eabd7342.
[14] Z. Shen, D. Fan, H. Zhang, et al., Sol. RRL 6 (2022) 2200483.
[15] F. Guo, B. Hu, C. Yang, et al., Adv. Mater. 33 (2021) e2101466.
[16] W.J. Ong, L.L. Tan, Y.H. Ng, S. Yong, S. Chai, Chem. Rev. 116 (2016) 7159–7329.
[17] X. Zhao, Q. Liu, X. Li, H. Ji, Z. Shen, Chin. Chem. Lett. 34 (2023) 108306.
[18] Y. Liao, J. Yang, G. Wang, et al., Rare Met. 41 (2022) 396–405.
[19] J. Zhao, X. Liu, Y. Zhou, T. Zheng, Y. Tian, Chin. Chem. Lett. 34 (2023) 107895.
[20] P. Li, G. Guan, X. Shi, et al., Rare Met. 42 (2023) 1249–1260.
[21] R. Li, X. Ma, J. Li, et al., Nat. Commun. 12 (2021) 1587.
[22] W. Yang, Z. Ni, D. You, et al., Rare Met. 42 (2023) 2577–2591.
[23] J. Huang, M. Wang, X. Zhang, et al., J. Alloys Compd. 923 (2022) 166256.
[24] G. Li, N. Li, S. Peng, et al., Adv. Energy Mater. 11 (2020) 2002721.
[25] J. Xiao, J. Zhao, X. Ma, et al., J. Alloys Compd. 889 (2021) 161542.
[26] Z. Wu, C. Li, Z. Li, et al., ACS Nano 15 (2021) 5696–5705.
[27] H. Jiang, C. Zang, Y. Zhang, et al., Catal. Sci. Technol. 10 (2020) 5964–5972.
[28] L.C. Makola, S. Moeno, C.N.M. Ouma, et al., J. Alloys Compd. 916 (2022) 165459.
[29] H. Cheng, W. Zhao, Friction 10 (2021) 398–410.
[30] L. Wang, Y. Li, P. Han, Sci. Rep. 11 (2021) 22950.
[31] N. Ma, Q. Fu, Y. Hong, et al., ACS Appl. Mater. Interfaces 12 (2020) 18165–18173.
[32] X. Zhou, Y. Guo, F. Zhao, et al., Adv. Mater. 32 (2020) 2007012.
[33] Y. Zou, P. Yang, L. Yang, et al., Polymer 217 (2021) 123464.
[34] X. Zhu, M. Li, L. Song, X.F. Zhang, J. Yao, Sep. Purif. Technol. 281 (2022) 119912.
[35] J. Yang, Y. Chen, X. Jia, et al., ACS Appl. Mater. Interfaces 12 (2020) 47029–47037.
[36] W. Li, X. Li, J. Liu, et al., ACS Appl. Mater. Interfaces 13 (2021) 22845–22854.
[37] Q. Zhang, L. Li, B. Jiang, et al., ACS Appl. Mater. Interfaces 12 (2020) 28179–28187.
[38] X. Chen, S. He, M.M. Falinski, et al., Energy Environ. Sci. 14 (2021) 5347–5357.
[39] Z. Li, M. Zheng, N. Wei, et al., Sol. Energy Mater. Sol. Cells 205 (2020) 110254.
[40] G. Zhao, Y. Chen, L. Pan, et al., Sol. Energy 233 (2022) 134–141.
[41] W. Li, F. Li, D. Zhang, F. Bian, Z. Sun, Wood Sci. Technol. 55 (2021) 625–637.
[42] Y. Wu, J. Chen, H. Che, et al., Appl. Catal. B: Environ. 307 (2022) 121185.
[43] L. Chen, X.-X. He, Z.-H. Gong, et al., Rare Met. 41 (2022) 2429–2438.
[44] Y. Zhang, Y. Wu, L. Wan, et al., Green Energy Environ. 7 (2022) 1377–1389.
[45] L. Wei, J. Li, C. Zhou, et al., Chin. Chem. Lett. 34 (2023) 107893.
[46] Z. Li, H. Fang, Z. Chen, et al., Appl. Catal. B: Environ. 312 (2022) 121374.
[47] C. Zhao, C. Ding, C. Han, X. Yang, J. Xu, Sol. RRL 5 (2020) 2000486.
[48] K. Zhou, W.L. He, X. Zhang, et al., Rare Met. 40 (2021) 799–807.